Inducing quantum phase transitions in nontopological insulators via atomic control of substructural elements

Thomas K. Reid [1], S. Pamir Alpay [1,2], Alexander V. Balatsky [2,3] and Sanjeev K. Nayak [1,2,*]

[1] *Department of Materials Science and Engineering and Institute of Materials Science, University of Connecticut, Storrs, Connecticut 06269, USA*

[2] *Department of Physics, University of Connecticut, Storrs, Connecticut 06269, USA*

[3] *NORDITA, KTH Royal Institute of Technology and Stockholm University, Stockholm SE-106 91, Sweden*

(Received 12 April 2023; revised 17 July 2023; accepted 2 November 2023; published 4 December 2023)

Topological insulators are an important family of quantum materials that exhibit a Dirac point (DP) in the surface band structure but have a finite band gap in bulk. A large degree of spin-orbit interaction and low band gap is a prerequisite for stabilizing DPs on selective atomically flat cleavage planes. Tuning of the DP in these materials has been suggested via modifications to the atomic structure of the entire system. Using the example of As_2Te_3 and $ZnTe_5$, which are not TIs, we show that a quantum phase transition can be induced in atomically flat and stepped surfaces, for As_2Te_3 and $ZrTe_5$, respectively. This is achieved by establishing a framework for controlling electronic properties that is focused on local perturbations at key locations that we call substructural elements. We exemplify this framework through a unique method of isovalent sublayer anion doping and biaxial strain.

DOI: 10.1103/PhysRevB.108.235402

I. INTRODUCTION

Topological insulators (TIs) are materials that have topologically protected surface states characterized by the Dirac point (DP) that is robust to non-time-reversal perturbations [1–3]. A large degree of spin-orbit coupling (SOC) in these materials leads to entanglement of band extrema at the Fermi level, leading to interchange of atomic contributions to the band occupancy in the bulk, as compared to regular semiconductors. This effect manifests on the surface as a DP, which is characterized by a zero band gap, linear band dispersion, and momentum-spin locking of chiral spin order. Graphene is the first material where a DP was observed; however, for active applications, functionalized graphene is under active consideration [4,5]. TIs have the advantage of a richer chemical space to engineer their properties. Projected applications of TIs include superconducting materials, quantum computers, spintronic devices, and quantum anomalous Hall insulators, making it a fruitful topic for investigation [6–8].

Realizing these quantum effects in naturally existing materials is a major challenge. Thus, much of TI research is focused on either conceptualizing new materials or tuning the properties of known materials [9]. Initial studies on the physics of TIs centered around the binary AB-type or A_2B_3-type chalcogenides, which laid fertile groundwork for studies that continue on this class of materials today [10–21]. Density-functional theory (DFT) modeling with the scalar-relativistic Kohn-Sham Hamiltonian and perturbative SOC is sufficient to account for the surface physics of target materials [5,22]. As a consequence, many of these modern studies depend upon the use of DFT-based computational methods.

A secondary challenge lies in identifying the quantum phase in which a material exists and whether that specific phase is a TI. The three characteristics of a DP may be observed in the band structure of a traditional DFT calculation, thus reasonably confirming a material is a TI, but it is worth outlining some alternative identification methods. One is integrating the Berry curvature across the Brillouin zone to obtain the system's topological invariant—for a TI, the relevant invariant is Z_2 [23]. Another approach would be taking advantage of the spin-momentum locking that characterizes the TI surface state and seeking to confirm an association between charge current and spin polarization. In an experimental procedure, this can be achieved, for example, with a ferromagnetic electrode [24].

II. METHODOLOGY

Here, we decided to employ an evaluation of the electronic band structure of a traditional DFT calculation, using as our TI-identification criteria the three DP characteristics we outlined. The traditional DFT approach that we have employed is systematically used for studying the electronic structure and topological surface states of quantum materials. In recent studies, we have applied various density-functional approximations for the exchange-correlation term to a representative sample of the A_2B_3 binary pnictogenide chalcogenide (BPC) TI group [25]. Because of the quintuple layer (QL) structure of these materials, it is also necessary to consider the role of the van der Waals (vdW) interaction, which we incorporated via the dispersion-corrected parameters. We found a set of methodological rules that are generally suitable for the A_2B_3 group. These are as follows: the use of a slab model with six or more unit layers, the use of a vacuum thickness $\geqslant 15$ Å (eliminating surface-surface interactions), the use of the generalized

*sanjeev.nayak@uconn.edu

 ©2023 American Physical Society

gradient approximation with the vdW parametrization [generalized gradient approximation (GGA) + vdW], inclusion of SOC, and thorough optimization of geometry. We use the same principles here in the construction of our computational models. Our study is performed by using the Vienna *Ab Initio* Simulation Package [26,27], which is a standard DFT code.

In a recent *ab initio* study, Ref. [28], the authors have reasoned that the spin current density-functional theory (SCDFT), which provides a formulation of DFT for fermions in the effective external field produced by the SOC that renormalizes the electron-electron interaction [29,30], is a better approach to predict the onset of topological phase transition. However, we note that the difference in predicted band structure of SCDFT and DFT+SOC—the latter implemented in this work—is slight, and accounting for this difference is complicated by the introduction of several additional modeling parameters. The chemical doping problem, as studied in this work, introduces stronger electron-electron perturbation that practically overrides the minor improvement of SCDFT over the DFT+SOC method, bringing about only a small error with no change in the properties trend. Our modeling is thoroughly tested for the material systems under investigation, see Refs. [31,32], and thus our results are valid.

III. RESULTS AND DISCUSSION

Using these very same tools, we have shown that thermoelectric non-TI semiconductor As_2Te_3 undergoes a quantum phase transition, becoming a TI, when subject to 1% strain in the *ab* plane. This is due to a Poisson effect, whereby the slab thickness undergoes a reduction in response to the extension of a and b; we further demonstrated the disproportionate contribution of the vdW gaps (d_{vdW}), which are "stacked" along c, in producing this reduction [32,33]. In addition, a correlation can be established with reduction in the outer atomic layer separation (d_{OAL}) toward control of TI functionality. Our study has shown that d_{OAL} can vary up to 11% for under conditions of $\pm3\%$ strain, which matches well to experiments performed on surface C-doped Bi_2Se_3, which report 10.7% variation [34,35]. From first-principles calculations it was shown that control over the TI properties can be achieved in the $Pb_{1-x}Sn_xTe$ solid solution, which possesses the rocksalt crystal structure throughout the composition range $0 \leqslant x \leqslant 1$, via application of hydrostatic strain [36].

Given that biaxial strain can only be readily induced by substrate lattice mismatch, the degree of strain is naturally dependent on the selection of a suitably mismatched substrate. A meaningful evolution of the standard method of analyzing the atomic structure of BPCs, which has primarily focused on "whole-system" structural features such as the number of quintuple layers (QLs), the overall thickness, and the orientation of the sample, can be found by focusing upon parameters such as the outermost d_{vdW} (d_{OvdW}) and d_{OAL}, which has important implications. In the As_2Te_3 case, by focusing on d_{OvdW} alone, we were able to observe that a single subfeature of the atomic structure could have an outsize, and indeed primary, impact on the band gap [33,37]. It thus became apparent that band gap tuning in BPCs could be made possible by careful mediation of substructural elements (SSEs) like the d_{OvdW} and d_{OAL}. While external strain factors into wholesome mechanical response to the electronic structure, an internal and localized "chemical" strain is an equally powerful method for modifying materials properties, and is not bound by such restrictions [36]. In this aspect, doping is a viable option and, with respect to the given problem, one looks forward to controlling the interlayer separation by isovalent doping to minimize changes to the bonding type. Overall, its advantages are numerous. Firstly, it introduces structural changes intrinsically, avoiding dependencies like lattice-mismatch strain. Secondly, it provides control over the chemistry of the system. And lastly, the structural perturbations are of local order.

Subsequently, we sought to explore this premise in two ways: (a) finding a method that demonstrates the feasibility of modifying SSEs in practice and (b) demonstrating the primacy of certain SSEs in determining electronic properties, like the band gap, in layered TI and TI-adjacent (DFT) together with spin-orbit interaction and report success in both pursuits [32]. Altogether, we show that a unique approach of sublayer isovalent anion doping (SIAD) and controlling dopant concentration offers major control over properties-relevant SSEs in As_2Te_3, and that the sublayer doping approach could be extended to stepped surfaces. For the stepped surface case, we chose to work on $ZrTe_5$, in which we achieved total band gap closure by substitutional doping at singular atomic sites.

In previous work, we studied the 6-QL As_2Te_3 slab constructed from the $R\bar{3}m$ unit cell [33]. Now, we present the results of the application of our doping strategy to this material. First, we built a set of models corresponding to 16 doping scenarios. For the chemistry of the dopant, we designated tellurium-isovalent elements S and Se, which we substituted at the fifth atomic layer (the lowest atomic layer of the outermost QL) and the sixth atomic layer (the highest atomic layer of the second QL), with the understanding that layer 5 and layer 6, although made up of the same element, i.e., Te, are symmetrywise inequivalent. This is schematically illustrated in Fig. 1(a). Each As_2Te_3 slab possesses a 2×2 reciprocity in the *ab* plane, which served to assess the effect of dopant concentration. For both dopants, at both the fifth and sixth layer, tellurium substitution proceeded progressively, with a model created for one, two, three, and four tellurium atoms replaced.

We examined a set of SSEs in comparison to the dopant site and concentration: d_{OvdW}, the thickness of the outermost QL (d_{OQL}), and the separation between the two outermost atomic layers (d_{OAL}). In order to simplify the comparison between the original and doped structures, we refer to the change of d_{OvdW} and d_{OAL} (respectively, Δd_{OvdW} and Δd_{OAL}). This is shown in Table I. What is apparent is a major reduction in all three SSEs in comparison to the undoped As_2Te_3 slab, with the Δd_{OvdW} showing a particularly large negative response to sulfur in layer 5 at concentrations exceeding 75%. This would appear to demonstrate the utility of substitutional anion doping for controlling BPC atomic structure. A major reduction in the band gap from the undoped structure from 0.130 to -0.035 eV is achieved when sulfur is at 100% concentration in layer 5, with the other doping conditions inducing reductions of the band gap of various degrees that are less severe. The overall picture is clear: by targeting the anions surrounding d_{OvdW}, significant control over the vdW gap and surrounding SSEs can be exerted, which in turn exerts major negative pressure

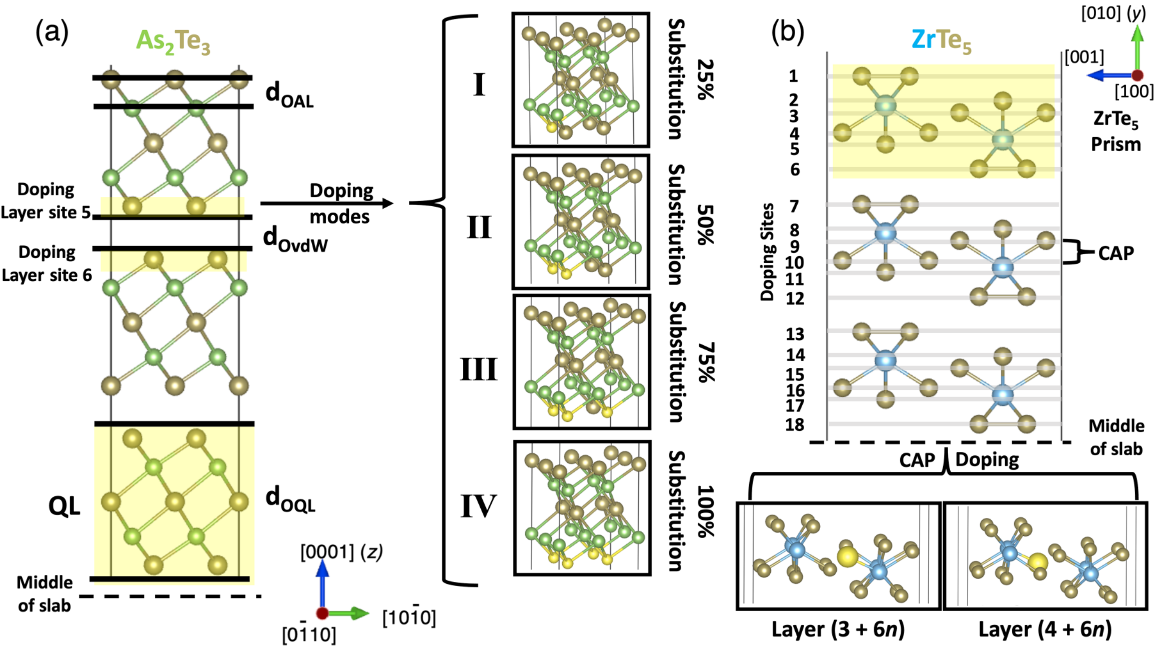

FIG. 1. Schematic representations of the As_2Te_3 (a) and $ZrTe_5$ (b) slab models are shown. Various structural parameters, defined according to our SSE-SIAD framework, are illustrated in relation to the structure, along with other features of note. In (a), the “doping layer site” labels correspond to the layers of Te atoms that were substituted to explore the effect of SIAD on the band structure, which are highlighted in yellow for additional clarity and to distinguish them from the SSEs d_{OAL}, d_{OvdW}, and d_{OQL}. In (b), CAP is identified at “doping sites” 9 and 10, but is present within all three $ZrTe_5$ “prisms” studied at layers $(3 + 6n)$ or $(4 + 6n)$ $\forall\, n \in 0,\ 1,$ and 2.

TABLE I. The band gap compared to structural parameters for S-doped As_2Te_3 models for different concentration of S in Te layer sites 5 and 6 [see Fig. 1(a)]. The structural parameters are presented in Δ, which is computed as the geometrically optimized state with dopants minus the optimized state of the corresponding pure model.

Layer concentration (%)	Band gap (eV)	Δd_{OQL} (Å)	Δd_{OAL} (Å)	Δd_{OvdW} (Å)
Doping S_{Te} on layer 5				
0	0.130	–	–	–
0.25	0.105	0.019	0.011	−0.212
0.50	0.059	0.144	−0.134	−0.365
0.75	0.060	0.207	0.039	−0.467
1.00	−0.032	−0.432	0.032	−0.431
Doping S_{Te} on layer 6				
0	0.130	–	–	–
0.25	0.118	−0.005	0.103	−0.188
0.50	0.109	−0.003	0.070	−0.354
0.75	0.129	−0.003	0.069	−0.456
1.00	0.012	−0.011	0.035	−0.363
Doping Se_{Te} on layer 5				
0	0.130	–	–	–
0.25	0.107	0.006	0.017	−0.141
0.50	0.102	0.068	−0.074	−0.296
0.75	0.084	0.111	0.136	−0.401
1.00	0.032	−0.247	0.033	−0.351
Doping Se_{Te} on layer 6				
0	0.130	–	–	–
0.25	0.115	−0.011	0.081	−0.138
0.50	0.118	−0.005	0.064	−0.280
0.75	0.127	0.014	0.064	−0.414
1.00	0.090	−0.013	0.032	−0.324

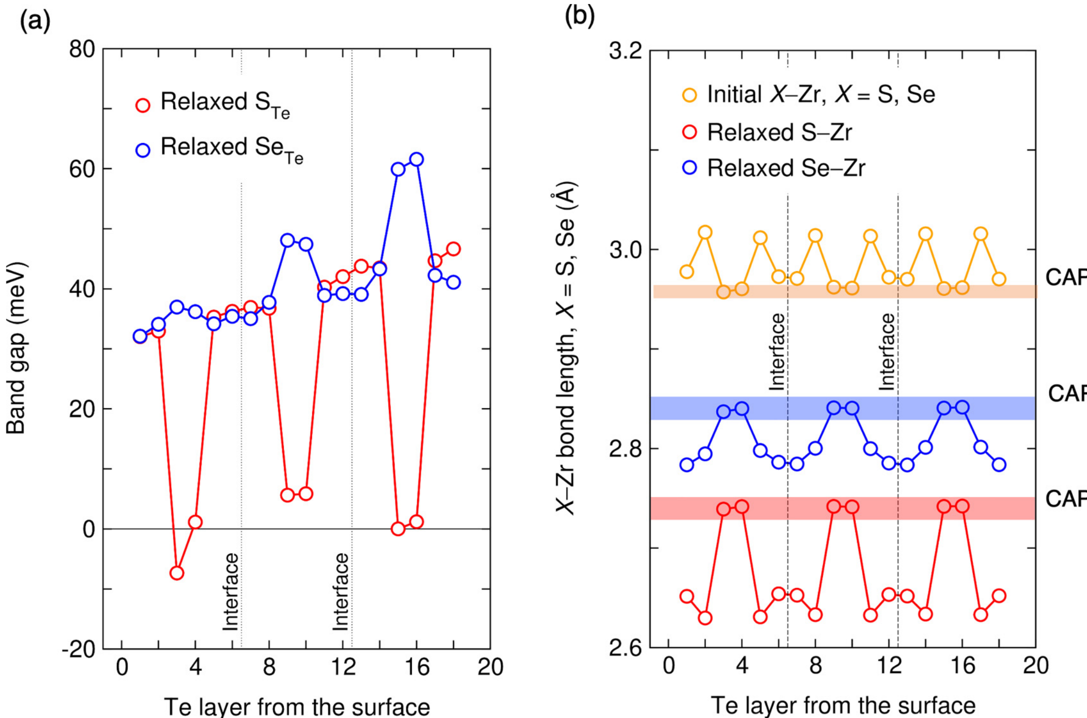

FIG. 2. The Te layer in $ZrTe_5$ for isovalent sulfur doping (S_{Te}) and isovalent selenium doping (Se_{Te}) is compared in (a) with the band gap and, in (b), with the bond length d_{S-Te} and d_{Se-Te}. The trapezoidal pattern evident in both sets of trend lines can be related to the repetition of the CAP SSE at layers $(3 + 6n)$ or $(4 + 6n)$ $\forall\ n \in 0,\ 1,$ and 2. The band gap was derived by occupancy analysis at the $\bar{\Gamma}$; see Refs. [32,36].

on the band gap, up to and including total band gap closure. Given that As_2Te_3 is a non-TI, we have further demonstrated that doping presents a plausible method for the transformation of non-TI BPCs into TIs, facilitated by an understanding of properties-relevant SSEs.

Due to the challenges currently surrounding its characterization as a TI, we decided to extend the hypothesis to $ZrTe_5$, which also possesses a distinct structure and stoichiometry. To accomplish this, we first constructed a set of 36 $ZrTe_5$ slab models, corresponding to 18 tellurium doping layer sites, for both sulfur and selenium dopants, each with 12-atom $ZrTe_5$ prisms. Each model, therefore, reflects substitutional doping of tellurium at one of the sites, with either sulfur or selenium. These doping layer sites proceed from the "top" of the material to the tellurium layer just "above" the central van der Waals gap (parallel to the *b* axis). All models possess 2×1 *ac*-plane reciprocation, and, at each layer site, 25% of the tellurium anions were replaced. These doping scenarios are schematically illustrated in Fig. 1(b). It must be noted that the $ZrTe_5$ (010) surface is "stepped," while the BPC (0001) surface is flat.

In Fig. 2(a), we show the relationship between the band gap of doped $ZrTe_5$, the layer site doped, and the dopant used. Firstly, we note that pristine, six-layer $ZrTe_5$ is a non-TI that maintains a band gap of 0.32 meV. This has been experimentally validated although the band gap value reported was lower than that we predicted [38,39]. It is apparent that a major negative response in the band gap occurs—total band gap closure, in nearly every case—when a sulfur dopant is located at layers $(3 + 6n)$ or $(4 + 6n)$ $\forall\ n \in 0,\ 1,$ and 2—these positions in the structure correspond to the sites in the $ZrTe_5$ structure which we designate the central anion pairs (CAPs), which are highlighted in Fig. 1(b). Conversely, we observe significant band gap opening with selenium doping. As such, we identify the CAP sites as a high-importance SSE in $ZrTe_5$ for tuning electronic properties. Figure 2(b) emphasizes this point, showing a strong relationship between the layer site doped, and postrelaxation changes to the various SSEs and the total thickness of the slab. Notably, the nearest-neighbor S–Zr bond length along the layers is smaller than the nearest-neighbor Se–Zr bond length. However, the CAP sites, where the *X*–Zr bond lengths are larger than other layers, are opposite in trend as compared to the undoped (initial) structure. By replacing a single anion in a structure of 144 atoms, we are able to achieve significant control of the band gap, so long as we target the correct SSE [see Fig. 3(b)]. We take special note that, in the case of Te layer site $(3 + 6n)$ and $(4 + 6n)$ sulfur doping, total or near-total band gap closure, a clear Dirac-like dispersion near the Γ point, and occupancy inversion is achieved according to the criteria of our previous work (see Refs. [32,36]).

To further validate the Z_2 nature of the surface states, we calculated the Chern number for the doped models. The Chern number, obtained by integrating the Berry curvature over a closed loop within the Brillouin zone, typically holds a value of 0 for conventional bands. However, it assumes integral values for topological surface states. In our investigation, we computed the Berry curvature utilizing the method of Fukui *et al.* [40], which is based on the wave functions, and executed it through the VASPBERRY code [41,42]. The Chern number analysis was performed for the lowest unoccupied bands associated with S doping at four distinct concentrations on Te layer

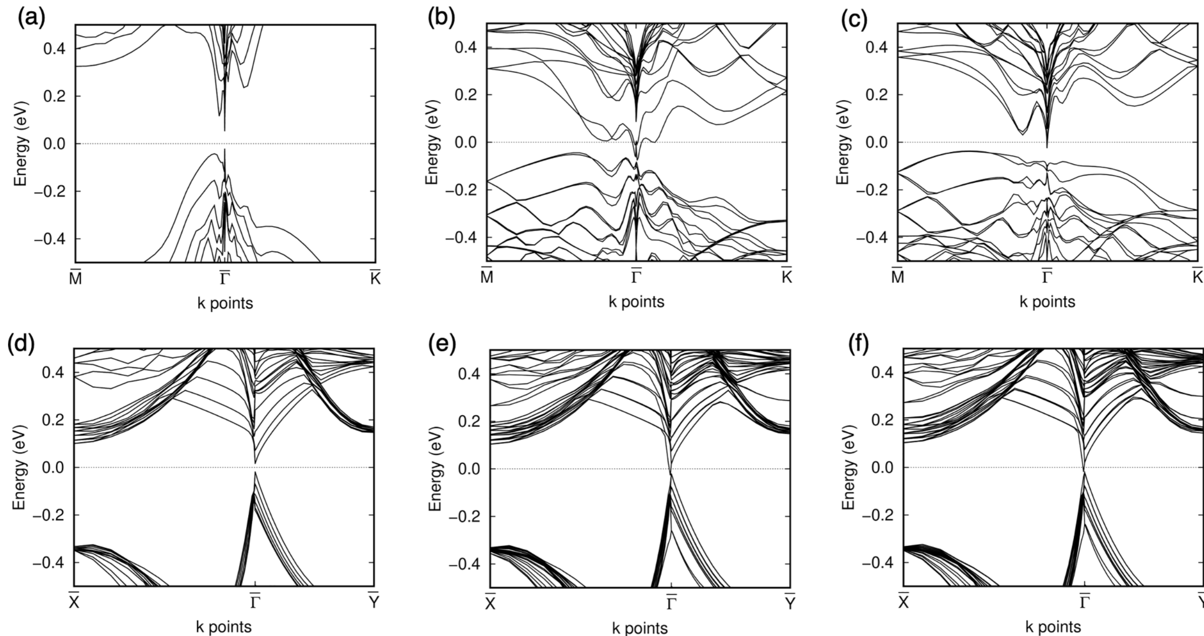

FIG. 3. Band structures for As_2Te_3 in (a)–(c) and $ZrTe_5$ (d)–(f). The undoped and 100% sulfur-doped cases for Te layer site 5 and Te layer site 6 in As_2Te_3 are represented in (a), (b), (c), respectively. The undoped and sulfur-doped cases on the Te site of layer 3 and atomic layer 4 (the CAP layers) of $ZrTe_5$ are represented in (d), (e), (f), respectively. In both cases, sulfur doping achieves total or significant band gap closure (see Table I for cross reference).

site 5, in conjunction with the undoped As_2Te_3 reference slab. The outcomes of these computations are tabulated in Table II. Our observations show that, except for the 100% S-doped case at Te layer site 5, which yielded a Chern number of 1, all other compositions exhibit a Chern number of 0. The integer value obtained for the 100% S-doping case at Te layer site 5 signifies the Z_2 topological nature of the surface state. This finding aligns perfectly with the insights drawn from Table I, wherein 100% substitution of S on Te layer site 5 resulted in a negative band gap and linear band dispersion near the Γ point—both characteristics of a topological surface state (TSS).

Similarly, the Chern number evaluation for S doping at the CAP of Te layer site 3 and Te layer site 4 yielded a value of 1, contrasting with the zero Chern number observed for the reference undoped $ZeTe_5$ slab. Notably, the "TSS?" column in Table II corroborates that the conclusions drawn from the parameters under consideration impeccably match the Z_2 topological nature, as discerned through the Berry curvature analysis. Thus the Chern number determination, in conjunction with the distinctive descriptors we employed, consistently affirm the Z_2 topological nature of the SS under investigation.

In summary, in contrast to a focus on whole-system properties like the total thickness and global strain, the use of high-impact SSEs facilitates materials design through targeted techniques like SIAD. In this study, the general importance

TABLE II. Chern number calculated using VASPBERRY code [41,42] on the surface band, i.e., lowest unoccupied band, for S doping at Te site with various concentrations in layer 5 of As_2Te_3. The column "TSS?" presents conclusions about the topology of the SS of the given model, based on the criterion that a TSS should exhibit a nonzero integer Chern number. Here, the condition of a TSS is designated as true (T), and a trivial surface state is designated as false (F). These conclusions match perfectly with the conclusions about the SS derived from Table I and Fig. 2.

As_2Te_3	Chern number of lowest unoccupied band	TSS?
S conc. in Te layer site 5 (in at. %)		
0	0	F
25	0	F
50	0	F
75	0	F
100	1	T
$ZrTe_5$		
No doping	0	F
Te layer site 3	1	T
Te layer site 4	1	T

of identification and control of SSEs for both As_2Te_3 and $ZrTe_5$ is clearly supported. Through the application of our doping strategy, we are able to achieve major control over the band gap of both materials with either atomic layer or single-atom substitutions at key structural sites. Specifically, we identified the d_{OvdW} and CAP sites for As_2Te_3 and $ZrTe_5$, respectively (see Fig. 1). In the $ZrTe_5$ case, this matches well to previous experimental and theoretical studies. It should be noted that, in both materials, it is sulfur that achieves band gap closure. In general, the band gap of TIs exhibits a sensitivity to various conditions like mechanical strain when material-specific constraints of nonmagnetic perturbation-robustness are overcome [38,39,43–46]. Our definition of TSS is negative band gap, pseudolinear dispersion, and integer Chern number. According to these criteria, we demonstrate, in this paper and the previous ones, switching between TSS and trivial surface states within the same material, for both natural trivial insulators and natural TIs.

IV. CONCLUSION

Our study emphasizes the potential for SSEs in TI and TI-adjacent materials to serve as a vehicle for the tuning of electronic properties. This can be achieved experimentally with advanced synthesis techniques like molecular beam epitaxy, selective ion implantation, and scanning-tunneling microscopy. Such an approach can be complemented by methods for modifying whole-system properties like biaxial strain to achieve an exact-zero band gap. In addition, due to the unique nature and experimental accessibility of the SSE-SIAD framework, we also verify the utility of a method for control over the electronic state of TIs and TI-adjacent materials in an experimental setting. Together, these insights indicate a promising course for the study and development of the next generation of TI-based applications.

The data that support the findings of this study are available within the article.

ACKNOWLEDGMENTS

The authors are grateful for the computational resources provided by the University of Connecticut. A.V.B. acknowledges the support by the European Research Council under the European Union Seventh Framework Grant No. ERS-2018-SYG 810451 HERO, and the Knut and Alice Wallenberg Foundation Grant No. KAW 2019.0068.

[1] B. Bradlyn, L. Elcoro, J. Cano, M. G. Vergniory, Z. Wang, C. Felser, M. I. Aroyo, and B. A. Bernevig, Topological quantum chemistry, Nature (London) **547**, 298 (2017).

[2] M. Z. Hasan and C. L. Kane, Colloquium: Topological insulators, Rev. Mod. Phys. **82**, 3045 (2010).

[3] S. Gupta and A. Saxena, A topological twist on materials science, MRS Bull. **39**, 265 (2014).

[4] S. Sahoo, S. L. Suib, and S. P. Alpay, Graphene supported single atom transition metal catalysts for methane activation, Chem. Cat. Chem. **10**, 3229 (2018).

[5] S. Sahoo, M. E. Gruner, S. N. Khanna, and P. Entel, First-principles studies on graphene-supported transition metal clusters, J. Chem. Phys. **141**, 74707 (2014).

[6] T. O. Wehling, A. M. Black-Schaffer, and A. V. Balatsky, Dirac materials, Adv. Phys. **63**, 1 (2014).

[7] X.-L. Qi and S.-C. Zhang, Topological insulators and superconductors, Rev. Mod. Phys. **83**, 1057 (2011).

[8] F. Duncan and M. Haldane, Topological quantum matter, Int. J. Mod. Phys. B **32**, 1830004 (2018).

[9] G. Aeppli, A. V. Balatsky, H. M. Rønnow, and N. A. Spaldin, Hidden, entangled and resonating order, Nat. Rev. Mater. **5**, 477 (2020).

[10] X. Yang, L. Luo, C. Vaswani, X. Zhao, Y. Yao, D. Cheng, Z. Liu, R. H. J. Kim, X. Liu, M. Dobrowolska-Furdyna, J. K. Furdyna, I. E. Perakis, C. Wang, K. Ho, and J. Wang, Light control of surface–bulk coupling by terahertz vibrational coherence in a topological insulator, npj Quantum Mater. **5**, 13 (2020).

[11] D. Flötotto, Y. Bai, Y.-H. Chan, P. Chen, X. Wang, P. Rossi, C.-Z. Xu, C. Zhang, J. A. Hlevyack, J. D. Denlinger, H. Hong, M.-Y. Chou, E. J. Mittemeijer, J. N. Eckstein, and T.-C. Chiang, *In situ* strain tuning of the Dirac surface states in Bi_2Se_3 films, Nano Lett. **18**, 5628 (2018).

[12] M. Safdar, Q. Wang, M. Mirza, Z. Wang, K. Xu, and J. He, Topological surface transport properties of single-crystalline SnTe nanowire, Nano Lett. **13**, 5344 (2013).

[13] T. H. Hsieh, H. Lin, J. Liu, W. Duan, A. Bansi, and L. Fu, Topological crystalline insulators in the SnTe material class, Nat. Commun. **3**, 982 (2012).

[14] S. M. Young, S. Chowdhury, E. J. Walter, E. J. Mele, C. L. Kane, and A. M. Rappe, Theoretical investigation of the evolution of the topological phase of Bi_2Se_3 under mechanical strain, Phys. Rev. B **84**, 085106 (2011).

[15] S. S. Hong, W. Kundhikanjana, J. J. Cha, K. Lai, D. Kong, S. Meister, M. A. Kelly, Z.-X. Shen, and Y. Cui, Ultrathin topological insulator Bi_2Se_3 nanoribbons exfoliated by atomic force microscopy, Nano Lett. **10**, 3118 (2010).

[16] Y. Zhang, K. He, C.-Z. Chang, C.-L. Song, L.-L. Wang, X. Chen, J.-F. Jia, Z. Fang, X. Dai, W.-Y. Shan, S.-Q. Shen, Q. Niu, X.-L. Qi, S.-C. Zhang, X.-C. Ma, and Q.-K. Xue, Crossover of the three-dimensional topological insulator Bi_2Se_3 to the two-dimensional limit, Nat. Phys. **6**, 584 (2010).

[17] P. Tsipas, E. Xenogiannopoulou, S. Kassavetis, D. Tsoutsou, E. Golias, C. Bazioti, G. P. Dimitrakopulos, P. Komninou, H. Liang, M. Caymax, and A. Dimoulas, Observation of surface Dirac cone in high-quality ultrathin epitaxial Bi_2Se_3 topological insulator on AlN(0001) dielectric, ACS Nano **8**, 6614 (2014).

[18] H. Zhang, C.-X. Liu, X.-L. Qi, X. Dai, Z. Fang, and S.-C. Zhang, Topological insulators in Bi_2Se_3, Bi_2Te_3, and Sb_2Te_3 with a single Dirac cone on the surface, Nat. Phys. **5**, 438 (2009).

[19] C. Schindler, C. Wiegand, J. Sichau, L. Tiemann, K. Nielsch, R. Zierold, and R. H. Blick, Strain-induced Dirac state shift in

topological insulator Bi_2Se_3 nanowires, Appl. Phys. Lett. **111**, 171601 (2017).
[20] J. Liu, W. Duan, and L. Fu, Two types of surface states in topological crystalline insulators, Phys. Rev. B **88**, 241303(R) (2013).
[21] Y. Tanaka, Z. Ren, T. Sato, K. Nakayama, S. Souma, T. Takahashi, K. Segawa, and Y. Ando, Experimental realization of a topological crystalline insulator in SnTe, Nat. Phys. **8**, 800 (2012).
[22] S. Sahoo, A. Hucht, M. E. Gruner, G. Rollmann, P. Entel, A. Postnikov, J. Ferrer, L. Fernández-Seivane, M. Richter, D. Fritsch, and S. Sil, Magnetic properties of small Pt-capped Fe, Co, and Ni clusters: A density functional theory study, Phys. Rev. B **82**, 054418 (2010).
[23] C. L. Kane and E. J. Mele, Z_2 topological order and the quantum spin Hall effect, Phys. Rev. Lett. **95**, 146802 (2005).
[24] W. Han, S. Maekawa, and X.-C. Xie, Spin current as a probe of quantum materials, Nat. Mater. **19**, 139 (2020).
[25] S. Grimme, J. Antony, S. Ehrlich, and H. Krieg, A consistent and accurate *ab initio* parametrization of density functional dispersion correction (DFT-D) for the 94 elements H–Pu, J. Chem. Phys. **132**, 154104 (2010).
[26] G. Kresse and J. Furthmüller, Efficiency of *ab-initio* total energy calculations for metals and semiconductors using a plane-wave basis set, Comput. Mater. Sci. **6**, 15 (1996).
[27] G. Kresse and J. Furthmüller, Efficient iterative schemes for *ab initio* total-energy calculations using a plane-wave basis set, Phys. Rev. B **54**, 11169 (1996).
[28] W. P. Comaskey, F. Bodo, A. Erba, J. L. Mendoza-Cortes, and J. K. Desmarais, Role of spin currents on electron-electron interaction in the quantum spin Hall phase, Phys. Rev. B **106**, L201109 (2022).
[29] G. Vignale and M. Rasolt, Current- and spin-density-functional theory for inhomogeneous electronic systems in strong magnetic fields, Phys. Rev. B **37**, 10685 (1988).
[30] K. Bencheikh, Spin–orbit coupling in the spin-current-density-functional theory, J. Phys. A: Math. Gen. **36**, 11929 (2003).
[31] E. Trushin and A. Görling, Spin-current density-functional theory for a correct treatment of spin-orbit interactions and its application to topological phase transitions, Phys. Rev. B **98**, 205137 (2018).
[32] T. K. Reid, S. P. Alpay, A. V. Balatsky, and S. K. Nayak, First-principles modeling of binary layered topological insulators: Structural optimization and exchange-correlation functionals, Phys. Rev. B **101**, 085140 (2020).
[33] T. K. Reid, S. K. Nayak, and S. P. Alpay, Strain-induced surface modalities in pnictogen chalcogenide topological insulators, J. Appl. Phys. **129**, 15304 (2021).
[34] S. Roy, H. L. Meyerheim, A. Ernst, K. Mohseni, C. Tusche, M. G. Vergniory, T. V. Menshchikova, M. M. Otrokov, A. G. Ryabishchenkova, Z. S. Aliev, M. B. Babanly, K. A. Kokh, O. E. Tereshchenko, E. V. Chulkov, J. Schneider, and J. Kirschner, Tuning the Dirac point position in Bi_2Se_3(0001) via surface carbon doping, Phys. Rev. Lett. **113**, 116802 (2014).
[35] S. Roy, H. L. Meyerheim, K. Mohseni, A. Ernst, M. M. Otrokov, M. G. Vergniory, G. Mussler, J. Kampmeier, D. Grützmacher, C. Tusche, J. Schneider, E. V. Chulkov, and J. Kirschner, Atomic relaxations at the (0001) surface of Bi_2Se_3 single crystals and ultrathin films, Phys. Rev. B **90**, 155456 (2014).
[36] M. Geilhufe, S. K. Nayak, S. Thomas, M. Däne, G. S. Tripathi, P. Entel, W. Hergert, and A. Ernst, Effect of hydrostatic pressure and uniaxial strain on the electronic structure of $Pb_{1-x}Sn_xTe$, Phys. Rev. B **92**, 235203 (2015).
[37] K. Shirali, W. A. Shelton, and I. Vekhter, Inter-quintuple layer coupling and topological phase transitions in the chalcogenide topological insulators, Electron. Struct. **5**, 15001 (2023).
[38] I. Mohelsky, J. Wyzula, B. A. Piot, G. D. Gu, Q. Li, A. Akrap, and M. Orlita, Temperature dependence of the energy band gap in $ZrTe_5$: Implications for the topological phase, Phys. Rev. B **107**, L041202 (2023).
[39] J. Mutch, W.-C. Chen, P. Went, T. Qian, I. Z. Wilson, A. Andreev, C.-C. Chen, and J.-H. Chu, Evidence for a strain-tuned topological phase transition in $ZrTe_5$, Sci. Adv. **5**, eaav9771 (2019).
[40] T. Fukui, Y. Hatsugai, and H. Suzuki, Chern numbers in discretized brillouin zone: Efficient method of computing (spin) Hall conductances, J. Phys. Soc. Jpn. **74**, 1674 (2005).
[41] H.-J. Kim, VASPBERRY: Berry curvature calculation code for VASP output, https://zenodo.org/records/1402593.
[42] S.-W. Kim, H.-J. Kim, S. Cheon, and T.-H. Kim, Circular dichroism of emergent chiral stacking orders in quasi-one-dimensional charge density waves, Phys. Rev. Lett. **128**, 046401 (2022).
[43] J. Wang, Y. Jiang, T. Zhao, Z. Dun, A. L. Miettinen, X. Wu, M. Mourigal, H. Zhou, W. Pan, D. Smirnov, and Z. Jiang, Magneto-transport evidence for strong topological insulator phase in $ZrTe_5$, Nat. Commun. **12**, 6758 (2021).
[44] H. Xiong, J. A. Sobota, S.-L. Yang, H. Soifer, A. Gauthier, M.-H. Lu, Y.-Y. Lv, S.-H. Yao, D. Lu, M. Hashimoto, P. S. Kirchmann, Y.-F. Chen, and Z.-X. Shen, Three-dimensional nature of the band structure of $ZrTe_5$ measured by high-momentum-resolution photoemission spectroscopy, Phys. Rev. B **95**, 195119 (2017).
[45] N. Aryal, X. Jin, Q. Li, A. M. Tsvelik, and W. Yin, Topological phase transition and phonon-space Dirac topology surfaces in $ZnTe_5$, Phys. Rev. Lett. **126**, 016401 (2021).
[46] P. Zhang, R. Noguchi, K. Kuroda, C. Lin, K. Kawaguchi, K. Yaji, A. Harasawa, M. Lippmaa, S. Nie, H. Weng, V. Kandyba, A. Giampietri, A. Barinov, Q. Li, G. D. Gu, S. Shin, and T. Kondo, Observation and control of the weak topological insulator state in $ZrTe_5$, Nat. Commun. **12**, 406 (2021).